RSC Advances

ROYAL SOCIETY OF CHEMISTRY

www.rsc.org/advances

Mechanistic and Stereoselective Study on the Reaction of Trifluoropyuvates with Arylpropenes Catalyzed by the Cationic Lewis Acid Rhodium Complex

Yang Wang, Xiaokang Guo, Bohua Wu, Donghui Wei*, and Mingsheng Tang*

The College of Chemistry and Molecular Engineering, Center of Computational Chemistry, Zhengzhou University, Zhengzhou, Henan Province, 450001, P.R. China

Abstract

The possible reaction mechanisms of stereoselective carbonyl-ene reaction between trifluoropyuvates and arylpropenes catalyzed by Lewis acid catalyst (Rh(III)-complex) have been investigated using the density functional theory (DFT). Six possible reaction pathways, including four Lewis acid-catalyzed reaction pathways and two noncatalyzed reaction pathways have been studied in this work. The calculated results indicate that the Lewis acid catalyzed reaction pathways are more energetically favorable than the noncatalyzed reaction pathways. For the Lewis acid-catalyzed pathways, there are four steps including complexation of catalyst with trifluoropyuvates, C-C bond formation, proton transfer, and decomplexation processes. Our computational outcomes show that the C-C bond formation step is both the rate- and enantioselectivity-determining step, and the reaction pathway leading to *S*-configured product is the most favorable pathway among the possible stereoselective pathways. The dication Rh(III)-complexes with different counterions (i.e., OTf^-, Cl^-, and BF_4^-) were considered as active catalysts, and the computed results indicate that the stereoselectivity can be improved with the presence of the counterion OTf^-. All these calculated outcomes align well with the experimental observations. Moreover, the stereoselectivity associated with the chiral carbon center is attributed to the lone pair delocalization and the variation in the stronger interaction. Furthermore, the analysis of global reactivity index has also been performed to explain the role of the Lewis acid catalyst.

Keywords: DFT, Mechanism, Enantioselectivity, Lewis acid

* Corresponding Authors: donghuiwei@zzu.edu.cn (D. H. Wei) and mstang@zzu.edu.cn (M. S. Tang)

1. Introduction

The carbonyl-ene reaction, which occurs between a carbonyl compound (the enophile) and an alkene with an allylic hydrogen (the ene), is a group-transfer reaction.[1] Generally, this transformation is a one-step manner and has a high barrier at the uncatalyzed condition,[2] and therefore it typically requires high temperature.[3] Since it features one of the simplest ways for C−C bond formation in syntheses, potentially 100% atom efficiency and high tolerance for ene and enophile variation, many efforts have been made toward the improvement and development of this kind of reaction.

Noteworthy, the Lewis acid-catalyzed carbonyl−ene reactions, which can afford high yields and stereoselectivities at the significantly lower temperature, have been widely used over the past decades. In 1988, Yamamato communicated the first asymmetric carbonyl−ene reaction catalyzed by modified Al-BINAP complexes.[4] Subsequently, Mikami published a series of studies of Ti-BINOL-catalyzed asymmetric glyoxylate/fluoral−ene reactions.[5] Then, more and more transition metal complexes derived from chiral ligands have also been employed in the catalysis of ene reactions. For example, Evans et al. reported the enantioselective carbonyl−ene reaction catalyzed by C_2-symmetric Cu(II)-bis(oxazolinyl) complexes.[6] Zheng and co-authors developed a novel chiral N,N′-dioxidenickel(II) complex to promote the asymmetric carbonyl−ene reaction.[7] Wang and co-workers discovered Rh(II)/Rh(III) carboxamidates can catalyze the carbonyl−ene reaction.[8] These transition-metal complexes can rival or even outperform non-transition-metal Lewis acids in terms of conversion, enantioselectivity, diastereoselectivity, and regioselectivity. Besides, the reactivities, stabilities and other important properties of the transition-metal catalysts can be controlled by systematic ligand modifications and/or variation of the metal center.

Recently, the pincer transition-metal complexes (e.g., M = Pd,[9] Ni,[10] Ru,[11] Pt,[12] Ir,[13] and Fe[14]) have been developed to be an important class of organometallic Lewis acid catalysts in asymmetric catalysis. Among them, the Rh-Phebox complexes have attracted more attention and exhibited excellent stereoselectivities in various catalytic asymmetric reactions, including the reductive aldol reactions, conjugate reductions, β-boration of α,β-unstaturated carbonyl compounds, and alkynylation of α-keto esters. Compared with Phebox ligands, Phebim ligands owe the advantage of further tunability of the electron density and steric bulkiness of the ligands

by appropriate choice of the substituent on the additional nitrogen atom. An outstanding example of the C_2-symmetric pincer rhodium(III) complexes serving as the Lewis acid to catalyze the asymmetric carbonyl-ene reaction of methyl trifluoropyruvate with 2-arylpropenes was firstly reported by Song's group (**Scheme 1**),[15] which deserves particular attention if we note the fact that the stereoselectivity of this reaction remains unsettled though carbonyl-ene reaction have been widely reported.

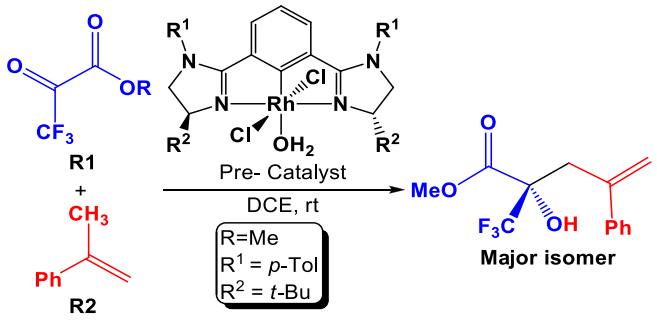

Scheme 1 The Lewis acid Rh(III)-complex catalyzed the title reaction

Different from the numerous studies in experiment, the theoretical investigations on the mechanism and stereoselectivity of this kind of reaction are rare. It should be noted that the novel reaction proceeding through either a one-step reaction or a stepwise mechanism with a zwitterionic intermediate and either C−C bond formation or proton transfer could be the rate-determining step are still debatable to date. For example, Zhang et al. adopted the one-step mechanism to disclose the influence of a variety of widely used Lewis acids (such as $AlCl_3$ and $SnCl_4$) on carbonyl-ene reactions.[16] Yamanaka and coworkers discovered very large asynchronicity and a significant amount of zwitterionic character in the one-step transition state structure as they studied the diastereoselectivity in $AlCl_3$- and $SnCl_4$-catalyzed carbonyl-ene reaction.[17] Bickelhaupt el al. theoretically demonstrated that the more polar the enophile is, the more asynchronous the ene reaction will be.[18] While Hang's group found that carbonyl enophile complexes followed a stepwise manner by using the kinetic isotope effect (KIE) determination.[19] Hillier et al. studied the bis(oxazoline) copper(II) complexes-catalyzed carbonyl−ene reactions using DFT and ONIOM methods and found that the reaction proceeds via a facile stepwise mechanism.[20] These studies are all concentrated on the mechanism of this novel reaction, but the factors that controlling the enantioselectivity are still unclear to date. To the best of our knowledge,

the computational investigation on the mechanism and enantioselectivity of Lewis acid Rh(III)−Phebim complex catalyzed carbonyl-ene reaction has also remained hitherto unsettled. With the complexity and ambiguity existence; theoretical investigations were desperately needed to make the mechanism more persuasive.

In this present study, we aim to disclose the mechanism and enantioselectivity of the Rh(III)-complex catalyzed carbonyl-ene reaction of methyl trifluoropyruvate with 2-arylpropenes as depicted in **Scheme 1**. As is known to all, for a multimolecular reaction, it is crucial to make clear which molecules are involved in each elementary step in order to access a complete understanding of the reaction mechanisms. Song and co-workers have conducted some efforts to propose the possible reaction mechanism, their explorations for this novel reaction are quite instructive but there are also some key issues that need to be settled: (1) For the keto-moiety, the ester carbonyl group not only renders the adjacent CF_3-substituted keto-group electron-deficient but also influences the coordinated conformation that the methyl trifluoropyruvate adopts. Bidentate coordination restricts rotation around the C−C bond that connects the two carbonyls and provides a more stereodefined complex that enhances the stereocontrol. Thus, which coordination mode is favorable for this reaction? (2) What is the real active species? (3) Is this Rh(III) complex catalyzed carbonyl-ene reaction stepwise or concerted? (4) Which is the rate-determining step in this reaction? (5) As the design of a new Lewis acid catalyst relies on a detailed understanding of the underlying factors that govern the enantioselectivity of these kinds of reactions, so what are the main factors that control the enantioselectivity of this reaction? With these puzzles as motivation, the present work will pursue a theoretical investigation on the title reaction to not only obtain a preliminary picture from the Lewis acid promoted carbonyl-ene reaction, but also explore the factors that control the stereoselectivity of this reaction. And we believe that the mechanistic information should be important for understanding the reaction and providing novel insights into recognizing this kind of reaction in detail.

For the sake of convenience, the reaction between trifluoropyuvate (**R1**, R = Me, **Scheme 1**) and phenylpropene (**R2**, **Scheme 1**) catalyzed by the Lewis acid Rh(III) complex catalyst (**Cat**, R^1 = *p*-tol, R^2 = *t*-Bu, **Scheme 2**) has been chosen as the object of investigation. In the present study, we will give the computational results for both of these possible reaction mechanisms at the molecular level using density functional theory (DFT), which has been widely used in the study of

organic,[21] biological reaction mechanisms,[22] and others.[23]

2. Computational details

Quantum mechanical calculations reported herein were carried out by using density functional theory with the *Gaussian 09* suite of programs.[24] The solution-phase geometry optimization of all species was performed with the gradient-corrected functional of Becke and Lee, Yang and Parr (B3LYP)[25] density functional for exchange and correction, along with the 6-31G* basis set for carbon, hydrogen, oxygen, nitrogen, and fluorine atoms. The SDD basis set,[26] as an effective core potential basis set, was used for rhodium atom. Solvent effects of dichloroethane (DCE, ε = 10.125), according to the experiment, were calculated through the SMD continuum solvation model developed by Truhlar and coworkers.[27] The harmonic vibrational frequency calculations were performed at the same level of theory as that used for geometry optimizations to provide thermal corrections of Gibbs free energies and to make sure that the local minima had no imaginary frequencies, while the saddle points had only one imaginary frequency. Intrinsic reaction coordinates (IRCs)[28] were calculated to confirm that the transition state structure connects the correct reactant and product on the potential energy surface, and the natural bond orbital (NBO)[29] analysis was employed to assign the atomic charges. The computed structures were rendered using the CYLView software.[30]

On the basis of the optimized structures at the B3LYP/6-31G*//SDD level in DCE solvent, the energies were then refined by B3LYP/6-311++G(2d,2p)//SDD single point calculations. The zero-point energies (ZPEs) and thermal corrections to free energies calculated at the B3LYP/6-31G*//SDD level were used to approximate those value of geometries optimized at the B3LYP/6-311++G(2d,2p)//SDD level. It should be noted that we will denote the computational method of geometry optimization at the B3LYP/6-31G*//SDD level as B3LYP/BS1, single point energy calculated at the B3LYP/6-311+G(2d, 2p) level B3LYP/BS2, and energy refinement with single-point energy calculated at the B3LYP/BS2 level plus ZPE or thermal correction calculated at the B3LYP/BS1 level as B3LYP/BS3.

Furthermore, the energies were also refined by single-point calculations using all electronic basis set def2-DZVP[31] using B3LYP, B3LYP-D3,[32] and M06-L[33] methods (see ESI). To date,

though with the increased availability of other methods, such as ωB97X-D and the Minnesota functionals, the dominance of B3LYP appears to be fading, the B3LYP is still one of the most popular and efficient methods. Moreover, the Stuttgart-Dresden (SDD) ECP with or without polarization functions has been confirmed to be reliable as it offers more flexibility in the valence shell, combined with a Pople style basis set (e.g., 6-31G* or 6-31G**) for main-group atoms.[34] As shown in **Table S1**, although the differences between the relative free energies of the key transition states computed at the other levels would become slightly smaller than those computed at the selected level, the same trend still can be obtained by using these methods. As concerned as above, we think the selected computational level should be proper and accurate enough for this catalytic system. All Gibbs free energies shown in this article were calculated at 1 atm and 298.15 K. Unless specified otherwise, all Gibbs free energies discussed in this paper were obtained at the B3LYP/BS3 level.

3. Results and Discussions

3.1. The mechanism protocol

3.1.1. The Lewis acid catalyzed reaction mechanism

On the basis of the presumptive mechanism proposed by Song, we suggested the possible catalytic cycle of the Lewis acid-catalyzed carbonyl-ene reaction (shown in **Scheme 2**): There are generally four steps in this catalytic cycle, including (1) the combination of methyl trifluoropyruvate with **Cat** via transition state **TS1** (Complexation process), (2) the reaction between another reactant 2-arylpropene and **M1** to give intermediate **M2** via transition state **TS2** (C−C bond formation process), (3) the intramolecular proton transfer process for the formation of intermediate **M3** via transition state **TS3** (Proton transfer process), and (4) the dissociation of the final product from the **Cat** via transition state **TS4** and the regeneration of **Cat** (Decomplexation process).

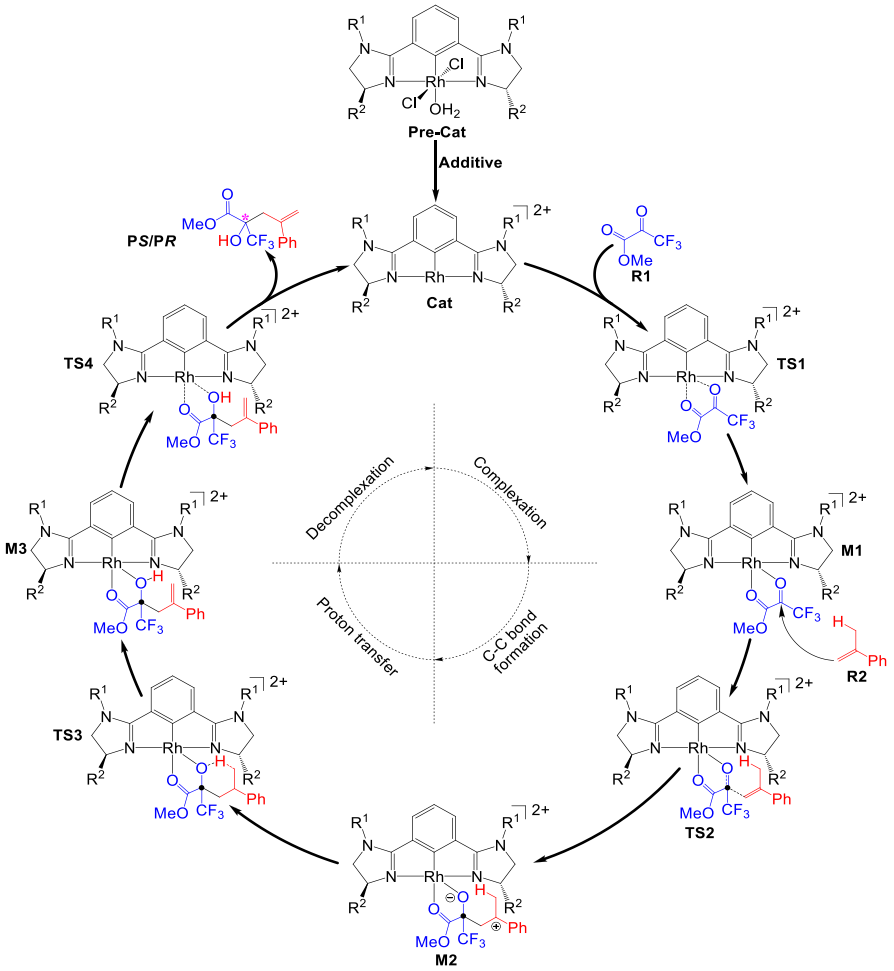

Scheme 2 The possible catalytic cycle of the title reaction

As stated in the Introduction, the complexation modes should be different due to the coordinated conformation that the methyl trifluoropyruvate adopts, thus, there are two complexation modes (*endo* and *exo*). It should be noted that we term the *endo* when the C3=O2 points on the axial position of the catalyst, whereas the C3=O2 pointing on the equatorial position of the catalyst is named *exo*. **Scheme 3** and **Fig. 1** present elementary step of the catalytic cycle and the free energy profiles of the entire fundamental channels, respectively. The detailed mechanistic discussions have been provided step by step.

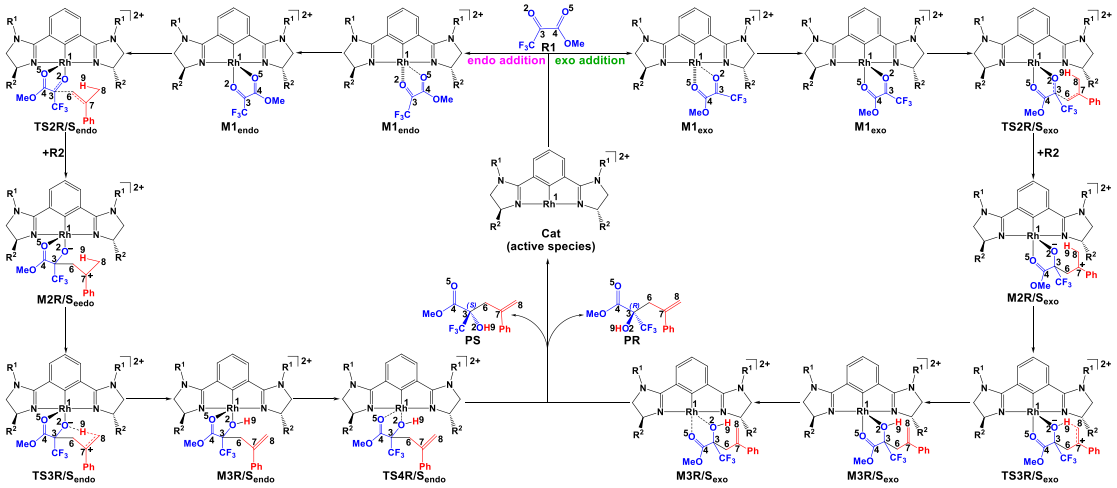

Scheme 3 The possible reaction mechanisms for each elementary step for the title reaction

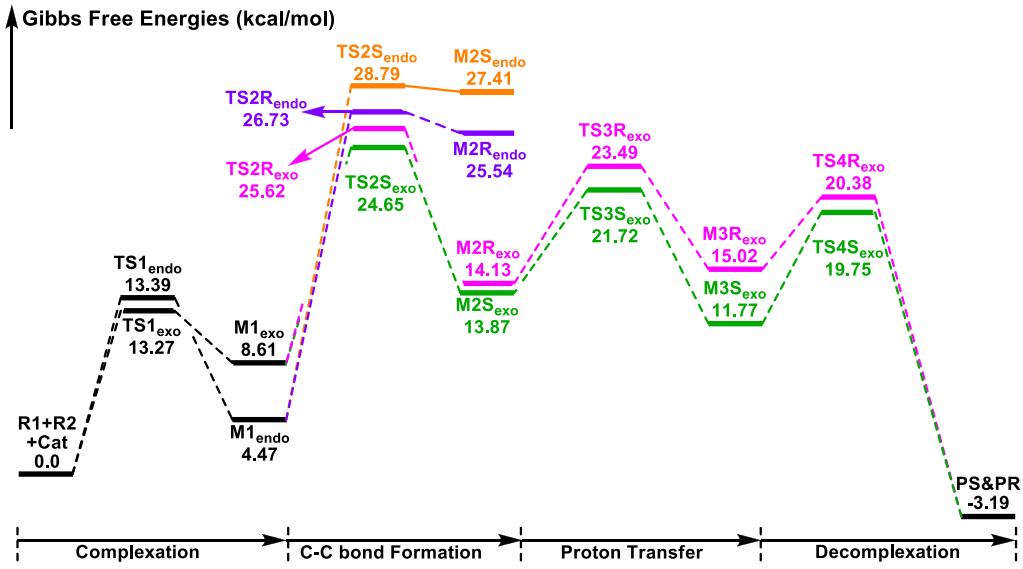

Fig. 1 The Gibbs free energies of the title reaction (units: kcal/mol)

First Step: the Complexation process. The first step is the formation of a catalyst-reactant complex between the methyl trifluoropyruvate (**R1**) and the Lewis acid catalyst (**Cat**). The different complexation patterns and different prochiral faces of catalyst-reactant complexes pose a considerable challenge from the computational point of view. The complexation of the Rh(III) center with two carbonyl oxygen atoms of **R1** initiates the catalytic reaction. The coordinated intermediates **M1**$_{exo}$ and **M1**$_{endo}$ are formed associated with transition states **TS1**$_{exo}$ and **TS1**$_{endo}$ through the coordinated conformation that the methyl trifluoropyruvate adopts (**Fig. 2**).

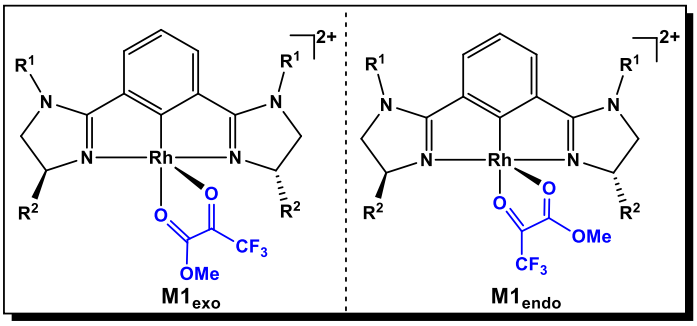

Fig. 2 Two different coordination modes

In the course of complexation, the partly filled *d*-orbitals of rhodium center accept electron from electron-rich carbonyl oxygen. As shown in **Fig. 3**, the distance of Rh1−O2 is shortened from 2.52/3.13 Å in **TS1**$_{exo}$/**TS1**$_{endo}$ to 1.99/2.80 Å in **M1**$_{exo}$/**M1**$_{endo}$, and the distance of Rh1−O5 is shortened from 3.14/2.49 Å in **TS1**$_{exo}$/**TS1**$_{endo}$ to 2.94/2.02 Å in **M1**$_{exo}$/**M1**$_{endo}$, respectively, which shows that accompanied with the electron transfer from **R1** to **Cat**, coordination bonds are formed via **TS1**$_{exo}$ and **TS1**$_{endo}$. The Gibbs free energy barriers of these two complexation processes via **TS1**$_{exo}$ and **TS1**$_{endo}$ (13.27 and 13.39 kcal/mol, **Fig. 1**) indicate that the reaction can occur under the experimental conditions.

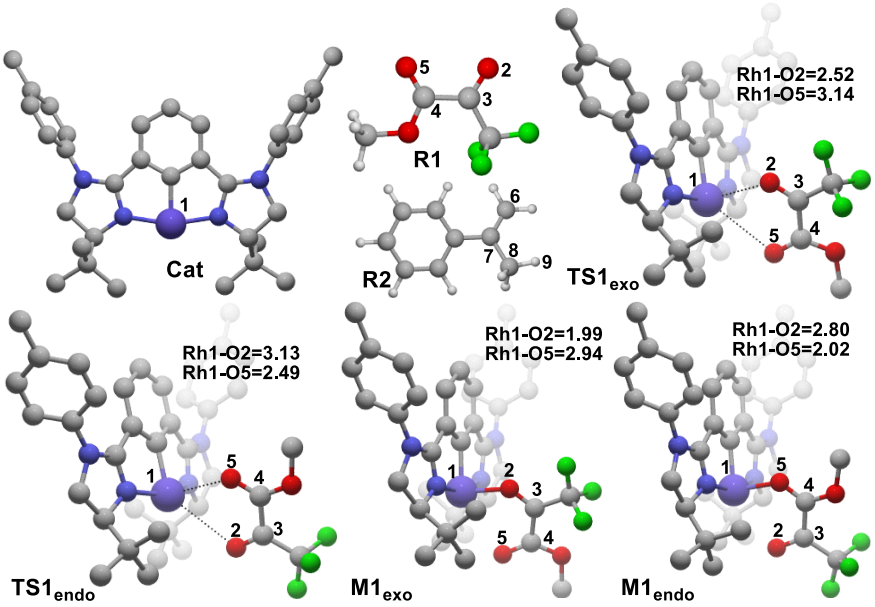

Fig. 3 The optimized structures involved in the first step. (Distances in Å) Most of the hydrogen atoms are omitted for sake of clarity. Gray, red, green, blue, white, and purple represent the carbon, oxygen, fluorine, nitrogen, hydrogen, and rhodium, respectively. Figures to be discussed below are represented using the same method.

Second Step: the C−C bond formation step. The second step is the addition of another reactant **R2** to **M1** (**M1**$_{exo}$ and **M1**$_{endo}$) for the formation of the zwitterionic intermediate **M2** via the C−C bond formation process. As shown in **Fig. 2**, the bidentate coordination restricts rotation around the C−C bond that connects the two carbonyls and provides a more stereodefined complex that enhances the stereocontrol. There exist four possible reaction patterns (**Scheme 4**) for the C−C bond formation process, because for either **M1**$_{exo}$ or **M1**$_{endo}$, **R2** can attack from either their *Re* or *Si* face to participate in the reaction. As an important note, the chirality center assigned on the C3 atom is formed during the C−C bond formation process, which depends on the *Re* or *Si* face of **M1**$_{exo/endo}$ that **R2** gets close to. The different attack mode on the prochiral C3 atom by **R2** determines the stereochemistry of the chirality of C3 atom center during the C−C bond formation step. It should be noted that the chirality center assigned on C3 atom is introduced in this step, which will be dominated as *R*/*S*. As can be seen in **Scheme 4**, the attack on *Re*-face of **M1**$_{exo}$ by **R2** affords the zwitterionic intermediate **M2*S***$_{exo}$ via **TS2*S***$_{exo}$, whereas the attack on *Si*-face of **M1**$_{exo}$ by **R2** gives the zwitterionic intermediate **M2*R***$_{exo}$ via **TS2*R***$_{exo}$. Similarly, the attack on *Si*-face of **M1**$_{endo}$ by **R2** affords **M2*R***$_{endo}$ via **TS2*R***$_{endo}$ whereas the attack on *Re*-face of **M1**$_{endo}$ by **R2** affords the **M2*S***$_{endo}$ via **TS2*S***$_{endo}$.

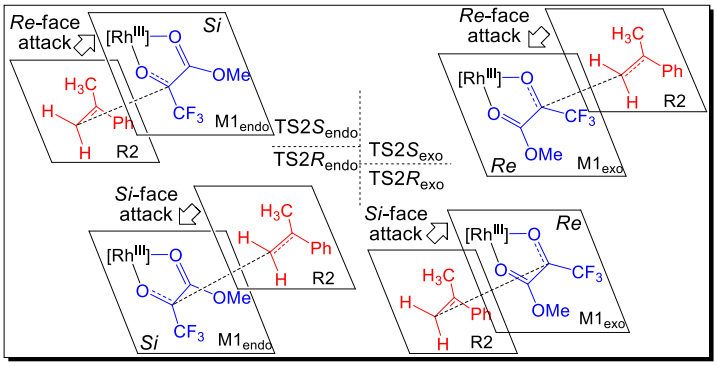

Scheme 4 Illustration of the stereochemistry

In the course of C3−C5 bond formation, with the approach of **R2** to the intermediate **M1**$_{exo}$/**M1**$_{endo}$, the electrostatic attraction between C3 and C5 will lead to complexes in either an *S* or *R* configuration, depending on which face of **M1**$_{exo/endo}$ that **R2** gets close to. Subsequently, the zwitterionic intermediate **M2*R*/*S***$_{exo/endo}$ is formed via transition state **TS2*R*/*S***$_{exo/endo}$, respectively. **Figure 4** describes the main geometrical structures for the four transition states and intermediates.

The changes of distance between C3 atom and C5 atom show that the C3−C5 bond is formed in this step. During the C−C bond forming process, the bond lengths of C8−H9 are 1.09~1.11 Å, which indicates that the ene reaction occurs via a stepwise manner. In the intermediate **M2**, the proton H9 is oriented toward to the O2 atom with the right relative conformation, which is necessary for the following proton transfer process. The free energy profile mapped in **Fig. 1** reveals that the energy barriers of the C−C bond formation process are 16.04 (**TS2*S*$_{exo}$**) and 17.01 (**TS2*R*$_{exo}$**) kcal/mol with respect to **M1$_{exo}$** for the *exo* addition, whereas these for *endo* addition are 22.26 (**TS2*R*$_{endo}$**) and 24.32 (**TS2*S*$_{endo}$**) kcal/mol with respect to **M1$_{endo}$**, respectively. Obviously, the *exo* addition pathway is more favorable than the *endo* addition pathway, thus in the following parts, we think it is unnecessary to discuss these two possible reaction pathways. The formation of **M2*S*$_{exo}$** costs the lowest energy barrier and the energy barrier of **TS2*S*$_{exo}$** is 0.97 kcal/mol lower than that of **TS2*R*$_{exo}$**, which indicates that the formation of **M2*S*$_{exo}$** is more energy favorable and supports the reported preference to form the *S*-configuration of the product.

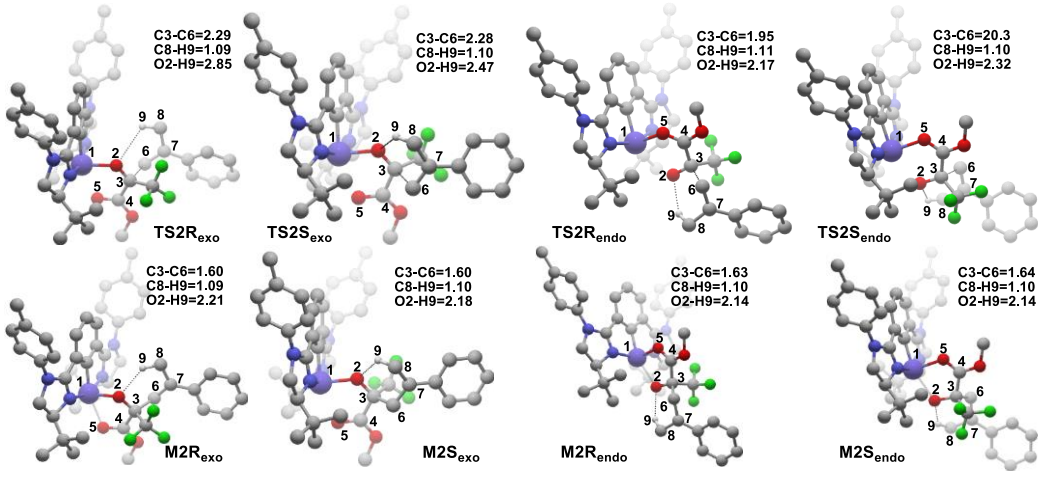

Fig. 4 The optimized structures involved in the second step. (Distances in Å)

Third Step: the proton transfer process. The subsequent step is the proton transfer process associated with the H9 transferring from C8 atom to O2 atom to form the intermediate **M3*R*$_{exo}$/M3*S*$_{exo}$** via transition state **TS3*R*$_{exo}$/M3*S*$_{exo}$**. The H9 atom on the C8 transfers to O2 atom through the six-membered ring transition structure **TS3*R*$_{exo}$/TS3*S*$_{exo}$**, in which the distances of O2−H9 and C8−H9 are 1.26/1.26 Å and 1.38/1.39 Å (**Fig. 5**), respectively. The length of the new formed O2−H9 bond is 0.99/0.99 Å in **M3*R*$_{exo}$/M3*S*$_{exo}$** showing the formation of O2−H9 bond. Moreover, the distance of Rh1−O2 is lengthened from 2.00/1.99 Å in **M2*R*$_{exo}$/M2*S*$_{exo}$** to 2.06/2.08

Å in **M3*R*$_{exo}$/M3*S*$_{exo}$**, which demonstrates that the coordination bond Rh1−O2 is weakened after the intramolecular proton transfer. This should be due to the electronic delocalization between Rh1 and O2 atoms. The free energy barriers calculated for this step (7.85 and 9.36 kcal/mol, **Fig. 1**) indicate that the proton transfer process is a facile process.

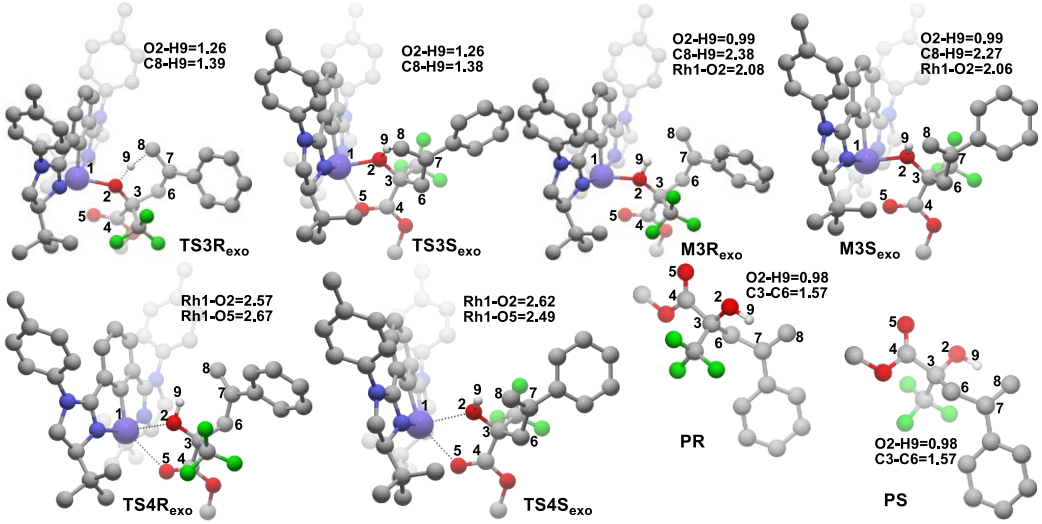

Fig. 5 The optimized structures involved in the third step. (Distances in Å)

Fourth Step: the regeneration of the catalyst. Since in the third step the homoallylic alcohol is formed, then the final step is the dissociation of the catalyst with product, and this leads to the regeneration of the catalyst. The transition state involved in this step is denoted as **TS4*R*$_{exo}$/TS4*S*$_{exo}$**. As shown in **Fig. 5**, the bond length of Rh1−O2 is increased form 2.08/2.06 Å in **M3*R*$_{exo}$/M3*S*$_{exo}$** to 2.57/2.62 Å in **TS4*R*$_{exo}$/TS4*S*$_{exo}$**, respectively. And the energy barriers of this step are 5.35 (**TS4*R*$_{exo}$**) and 7.98 (**TS4*S*$_{exo}$**) kcal/mol, which implies that the dissociation process is a facilitated process and the catalyst is easy to regenerate.

Furthermore, we have also considered the effects of the solvent (DCE) and counterions (i.e., OTf^-, Cl^-, and BF_4^-), and the results are summarized in **Table 1**. From **Table 1**, we found that the most active catalytic species is the dicationic Rh(III)-Phebim complex (**Cat**), which owns the lowest energy barrier. This phenomenon indicates the coordination of the counterions or solvent on the vacant orbital of the **Cat** reduces its electrophilic ability and lowers the activity of the catalyst, which is because the Rh(III)-Phebim complex is more stable by coordinated with the counterions. Though the coordinated Rh(III)-Phebim complex promoted the reaction is dynamically less favorable, the possibility of the Rh(III)-Phebim complex coordinated with

counterion catalyzed the reaction is also possible. The experimental results[15] show that the stereoselectivity is improved with the presence of OTf^- and our computational results also confirmed this tendency ($\Delta\Delta G^{\neq}$(**TS*R*$_{exo}$**−**TS*S*$_{exo}$**) = 2.36 kcal/mol, **Table 1**).

Table 1 The Gibbs free energy barriers of the C-C bond formation step catalyzed by different catalysts (units in kcal/mol)

Catalyst (L=bis(imidazolinyi)phenyl)	Reaction Pathway			
	exo addition		*endo* addition	
	S	R	R	S
RhL	13.64	15.26	18.70	21.51
RhL-OTf	21.55	23.91	24.57	27.31
RhL-BF_4	18.90	20.49	24.43	24.60
RhL-Cl	22.74	25.28	27.35	28.08
RhL-DCE	21.20	22.89	24.42	27.63

3.1.2. The direct reaction mechanism

To give more comprehensive understandings on the Rh(III)-Phebim complex catalyst, the un-catalyzed carbonyl-ene reaction channels (Channels A and B) have also been investigated. The proposed mechanism of the un-catalyzed carbonyl-ene reaction and the Gibbs free energy of the two transition states are depicted in **Scheme 5**. The calculated results show that the reaction occurs by a one-step fashion, which is remarkably different from the stepwise manner at the catalyzed condition.

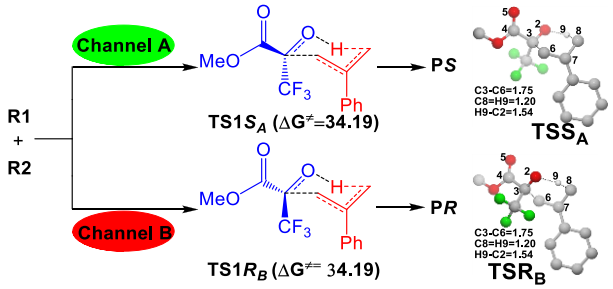

Scheme 5 The un-catalyzed carbonyl−ene reaction of trifluoropyuvates with arylpropenes

During the reaction, the H9 atom transfers from C8 to O2 along with the formation of C3−C6

bond via the six-membered ring transition states **TS1*S*$_A$** and **TS1*R*$_B$** to form the products **P*S*** and **P*R***, respectively, and the attack on the alternative face of **R1** by **R2** determines the chirality of C3 atom in the final product. The distance between C3 atom and C6 atom is shortened from 1.75 Å in **TS1*S*$_A$**/**TS1*R*$_B$** to 1.57 Å in **P*S***/**P*R***, concerted with that of O2−H8 is shortened from 1.20 Å in **TS1*S*$_A$**/**TS1*R*$_B$** to 0.98 Å in **P*S***/**P*R***. The free energy barriers via **TS1*S*$_{exo}$** and **TS1*R*$_{exo}$** are both 34.19 kcal/mol, which reveals that the reaction should be difficult to occur under the experimental conditions.

Having established the reaction mechanism of the title reaction, we now evaluate the bond order involved in the C-C bond formation step to disclose the difference between the catalytic and direct coupling reaction. The bond orders *P* nicely reflect the alteration of the C3−C6, C8−H9, and O2−H9 bonds. According to the results depicted in **Table 2**, the bond orders *P*(C8−H9) changes very tinny during the C-C bond formation process in the catalytic mechanism, which agrees with that the formation of C-C and O-H bonds occurs via a stepwise manner. The existence of the bond orders *P*(O2−H9) in **TS2**s and **M2**s is due to the formation of C-H…O hydrogen bond and thus weakens the C8−H9 σ bond. In contrast, the bond order *P*(C8−H9) decreases to 0.64, the bond orders *P*(O2−H9) and *P*(C3−C6) increase to 0.21 and 0.73 in the direct coupling reaction pathway respectively, indicating the formation of O2−H9 and C3−C6 bonds and the breaking of C8−H9 bond occur simultaneously. The bond orders clearly reveal that the reaction proceeds via different mechanisms under catalytic and un-catalytic conditions and these analyses are consistent with the above mechanistic studies.

Table 2 The Wiberg bond order *P* of the key bonds involved in the C-C bond formation step of the reaction at the B3LYP/6-31G*/SDD//SMD$_{(DCE)}$ level

	Bond Order		
	P(C3-C6)	*P*(C8-H9)	*P*(O2-H9)
R2	-	0.99	-
TS2*R*$_{exo}$	0.33	0.91	0.02
TS2*S*$_{exo}$	0.37	0.89	0.01
TS2*R*$_{endo}$	0.54	0.86	0.04
TS2*S*$_{endo}$	0.48	0.88	0.03
M2*R*$_{exo}$	0.91	0.87	0.02
M2*S*$_{exo}$	0.91	0.85	0.02
M2*R*$_{endo}$	0.86	0.85	0.04
M2*S*$_{endo}$	0.85	0.85	0.04

TS*R*$_{non}$	0.73	0.64	0.21
TS*S*$_{non}$	0.73	0.64	0.21

Taken together, one can conclude that the catalytic mechanism (**Scheme 3**) is obviously more favorable than the direct one (**Scheme 5**), and for the catalytic mechanism, the most favorable mechanism among the four steps is the *exo* addition associated with the *S*-configured isomer. The second step, i.e. addition of **R2**, is the rate- and enantioselectivity- determining step of the whole reaction associated with the energy barrier of 16.04 kcal/mol with respect to **M1**$_{exo}$. It also determines the enantioselectivities (*S* favorable) associated with the chiral carbon C3 atom.

3.2. The Origin of Enantioselectivity

As described above, the second step (C-C bond formation process) of the title reaction under the catalyzed condition is calculated to be the rate- and enantioselectivity-determining step. To obtain deep insights into the origins of the enantioselectivity of the target reaction, we then applied the NBO second-order perturbation analysis on transition states **TS2*S*$_{exo}$** and **TS2*R*$_{exo}$** to address this issue, which has been successfully used in organic reactions to explain the stereoselectivity,[35] could help us to evaluate intramolecular interactions. For each (*i*) donor and (*j*) acceptor, the second-order perturbation interaction energy can be expressed by the following equation: $E(2)=E_{ij}=q_iF_{ij}^2/\varepsilon_i\varepsilon_j$, where F_{ij} is the off-diagonal element in the NBO Fock matrix, q_i is the donor orbital occupancy, and ε_i and ε_j are diagonal elements (orbital energies).

Table 3 lists the donor-acceptor interactions involving the forming bonds in **TS2*S*$_{exo}$** and **TS2*R*$_{exo}$**. In **TS2*S*$_{exo}$**, the significant stabilization interaction is in favor of the C6 lone pair delocalization presented in **Table 3**, i.e. the delocalization of the C6 lone pair upon the π*(2) orbital of the O5-C4 bond with $E_{n\rightarrow\pi^*}$ = 323.89 kcal/mol. In the transition state **TS2*R*$_{exo}$**, the stabilization energies feature the same characteristic, the major contributions to the stabilization of **TS2*R*$_{exo}$** come from the delocalization of the C6 lone pair, namely, the n→π* between the lone pair of C6 and π*(2) orbital of the O5-C4 bond with $E_{n\rightarrow\pi^*}$ = 182.28 kcal/mol. Obviously, the lone pair delocalization energy in **TS2*R*$_{exo}$** is much lower than that in **TS2*S*$_{exo}$**, while the other stabilization interactions in **TS2*S*$_{exo}$** and **TS2*R*$_{exo}$** do not differ significantly. Results of the NBO analysis reinforce the importance of stereoelectronic effects, which contribute to the lower energy

of **TS2*S*$_{exo}$** relative to **TS2*R*$_{exo}$**.

Table 3 The second-order perturbation energy *E*(2) (kcal/mol) of donor-acceptor interactions in terms of forming bonds in **TS2*S*$_{exo}$** and **TS2*R*$_{exo}$**

TS2*S*$_{exo}$				**TS2*R*$_{exo}$**			
Donor	Acceptor	Interaction	*E*(2)	Donor	Acceptor	Interaction	*E*(2)
LP(1)C6	BD*(2)O5-C4	n-π*	323.89	LP(1)C6	BD*(2)O5-C4	n-π*	182.28
LP*(1)C8	BD*(2)O5-C4	n*-π*	9.23	BD(2)O5-4	LP(1)C6	π-n	5.19
BD(2)O5-C4	LP(1)C6	π-n	6.13	BD(1)C6-H11	BD*(2)O5-C4	σ-π*	3.58
BD(1)C6-H12	BD*(2)O5-C4	σ-π*	3.20	BD(1) C3-C4	LP(1)C6	σ-n	2.57
BD(1)C3-C4	LP (1)C6	σ-n	2.64	LP*(1)C8	BD*(2)O5-C4	n*-π*	2.26
BD(1)C6-H11	BD*(2)O5-C4	σ-π*	1.75	LP (1)C6	BD*(2)O2-C3	n-π*	1.95
BD(1)C8-C6	BD*(2)O5-C4	σ-π*	1.59	BD(1)C6-H12	BD*(2)O5-C4	σ-π*	1.55
BD(1)C4-C10	LP(1)C6	σ-n	1.30	BD(1)C8-6	BD*(2)O5-C4	π-π*	1.29
LP(1)C6	BD*(2)O2-C3	n-π*	1.09	BD(1)C4-C10	LP(1)C6	σ-n	1.23

In addition to the stereoelectronic effects, we have also performed the distortion/interaction reactivity analysis of the transition states **TS2*S*$_{exo}$** and **TS2*R*$_{exo}$**. The distortion/interaction analysis is a fragment approach to understand organic reactions, in which the height of the energetic barrier is described in terms of the original reactants. As depicted in **Fig. 6**, the activation energy of the transition states is decomposed into two main components: the distortion ($\Delta E_{dist}^{\neq}$) and the interaction ($\Delta E_{int}^{\neq}$) energy.[36] The distortion energy involves geometric and electronic changes to deform the reactants into their transition state geometry, which involves bond stretching, angle decrease or increase, dihedral changes and so on. The interaction energy contains repulsive exchange-repulsive and stabilizing electrostatic, polarization, and orbital effects in the transition state structure. The interaction energy is recovered by the relationship: $\Delta E_{int}^{\neq} = \Delta E^{\neq} - \Delta E_{dist}^{\neq}$.

The calculated distortion and interaction energies of the reactants in transition state geometries are listed in **Table 4**. For the two transition states **TS2*S*$_{exo}$** and **TS2*R*$_{exo}$**, the distortion energies of ene (**R2**) and Rh-trifluoropyuvate complex (**M1*$_{exo}$***) in the geometries are very similar: 5.68~8.26 kcal/mol for $\Delta E_{dist}^{\neq}$(**R2**) and 11.65~15.49 kcal/mol for $\Delta E_{dist}^{\neq}$(**M1$_{I}$**). However, the

interaction energies ($\Delta E_{int}^{\neq}$) of the two deformed reactants can be quite different for these two transition states. The $\Delta E_{int}^{\neq}$ of **TS2*S*$_{exo}$** is -22.76 kcal/mol, which is much more negative than that of the transition state leads to *R*-configured product (-16.01 kcal/mol for **TS2*R*$_{exo}$**). Apparently, the much stronger interaction energy between the deformed ene (**R2**) and Rh-trifluoropyuvate complex (**M1$_{exo}$**) in **TS2*S*$_{exo}$** makes it to be the most stabilized transition state for the formation of *S*-configured product.

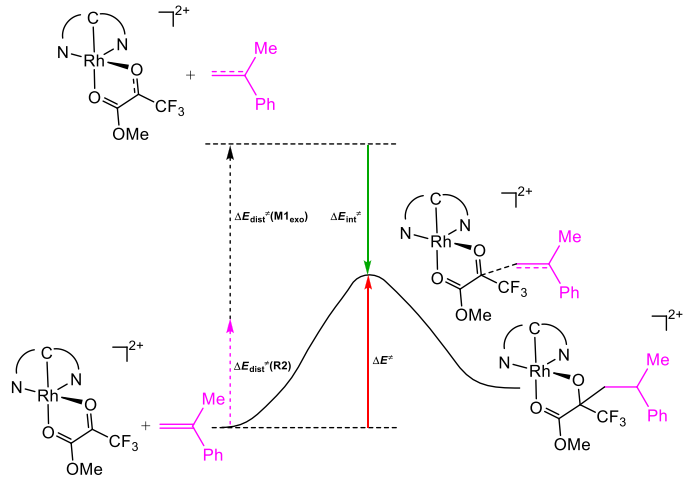

Fig. 6 The relationship between the activation energy and the distortion and interaction energies of reactants.

Table 4 The distortion/interaction reactivity analysis for the rate-determining step of the title reaction (All values are in kcal/mol).

TS	$\Delta E_{dist}^{\neq}$(**R2**)	$\Delta E_{dist}^{\neq}$(**M1$_{exo}$**)	$\Delta E_{int}^{\neq}$	$\Delta E^{\neq}$ [a]
TS2*S*$_{exo}$	8.26	15.49	-22.76	0.99
TS2*R*$_{exo}$	5.68	11.65	-16.01	1.32

Note: (a) The $\Delta E^{\neq}$ value is the calculated electronic energy of each transition state relative to the sum of the electronic energies of the two separate reactants.

As mentioned above, both the stereoelectronic effects and the stronger interaction energy between the deformed ene (**R2**) and Rh-trifluoropyuvate complex (**M1$_{exo}$**) play important roles in determining whether **TS2*S*$_{exo}$** is more energy favorable than **TS2*R*$_{exo}$**. The computed energy difference between **TS2*S*$_{exo}$** and **TS2*R*$_{exo}$** is 0.97 kcal/mol, which corresponds to an enantiomeric

excess of 67% in favor of the *S* isomer. This prediction is in good accordance with the experimentally observed *ee* of 77%. It should be noted that the energy of **R1+R2+Cat** is the lowest point in both the energy profiles of the two competitive pathways, and the energy barrier of the entire pathway should be the energy difference between the lowest reactants **R1+R2+Cat** and the corresponding highest energy transition state, so the energy span between the two competitive manifolds is still 0.97 kcal/mol, which is the same with the energy gap (0.97 kcal/mol) between the two highest energy transition states.

3.3. Role of the Lewis Acid Catalyst

In order to further understand the role of the catalyst Rh(III)-Phebim complex (**Cat**) in depth and compare the reactivity of the dicationic Rh (III) species with the cationic Rh(III)-counterion complex, we have performed the analysis of the global reactivity index (GRI) of the reactants before and after the absorption by catalyst. The molecule global electrophilicity character is measured by electrophilicity index, **ω**,[37] which has been given from the following expression, $\omega=(\mu^2/2\eta)$,[37-38] in terms of the electronic chemical potential **μ** and the chemical hardness **η**. Both quantities may be approached in terms of the one-electron energy of the frontier molecular orbital HOMO and LUMO, E_H and E_L, as $\mu\approx(E_H+E_L)/2$ and $\eta\approx(E_L-E_H)$. Moreover, according the HOMO energies obtained within the Kohn-Sham scheme,[39] Domingo and co-workers gave the nucleophilicity index **N** to handle a nucleophilicity scale.[40] The nucleophilicity index is defined as $N= E_{H(SR)}-E_{H(TCE)}$. This nucleophilicity scale is referred to tetracyanoethylene (**TCE**) taken as reference. Followed these indices definition, in this reaction (**Table 5**), **R2** is classified as the nucleophile with the nucleophilicity index of 2.590 eV. **R1** and **M1*exo*** are electrophiles with the value of 2.785 and 8.421 eV, respectively. Obviously, the coordination of catalyst **Cat** to carbonyl oxygen atom of **R1** noticeably strengthens the electrophilicity of **R1**, and thus lowers the free energy barrier of the carbonyl-ene reaction. The GRI analysis further revealed that the coordination of the counterions (*i. e.*, Cl^-, BF_4^-, TfO^-, DCE, and H_2O) cannot lower the energy barrier of the reaction, which is probably due to the lower acidity of the Lewis acid. These results further support the fact that the dicationic Rh(III)-Phebim complex (**Cat**) is the most active catalyst.

Table 5 Energies of HOMO (E_L ,a.u.) and LUMO (E_L, a.u.), Electronic Chemical Potential (μ,

a.u.), Chemical Hardness (η, a.u.), Global Electrophilicity (ω, eV), and Global Nucleophilicity (N, eV) of Some Reactants (SR)

SR	E_H (a.u.)	E_L (a.u.)	μ (a.u.)	η (a.u.)	ω (eV)	N[a] (eV)
R1	-0.288	-0.102	-0.195	0.186	2.785	0.778
R2	-0.221	-0.023	-0.122	0.198	1.024	2.590
M1*exo*	-0.243	-0.173	-0.208	0.070	8.421	1.997
M1*exo*-Cl (with counterion Cl^-)	-0.221	-0.143	-0.182	0.078	5.758	2.593
M1*exo*-BF_4 (with counterion BF_4^-)	-0.227	-0.152	-0.190	0.075	6.558	2.437
M1*exo*-OTf (with counterion TfO^-)	-0.226	-0.148	-0.187	0.078	6.066	2.473
M1*exo*-DCE (with solvent DCE)	-0.244	-0.162	-0.203	0.082	6.904	1.970

Note: [a] E_H(TCE)= – 0.31657 a.u. (calculated at B3LYP/6-31G(d)/SDD//IEF-PCM (DCE).

4. Conclusions

In this present study, we have analyzed the carbonyl-ene reaction between trifluoropyuvates (**R1**) and arylpropenes (**R2**) catalyzed by the Lewis acid catalyst Rh(III)−Phebim complex using density functional theory. Both of the catalyzed and un-catalyzed (Channels A and B) reaction mechanisms are considered. On the basis of our calculations, the Lewis acid catalyzed reaction is demonstrated to occur through four steps, and for each step, more than one possible pathway that involved different participation molecules has been investigated. The calculated results reveal that the exo addition pathway associated with *S*-configured isomer is the most favorable pathway among the six reaction pathways and the second step (C-C bond formation step) is the rate- and stereoselectivity-determining step. The enantioselectivity associated with the chiral carbon center (C3) atom turns out to be determined by the *Re* or *Si* face addition of **R2** with **M1**. All the calculations are in consistent with the experimental results.

Moreover, both the stereoelectronic effects and the stronger interaction energy between the

deformed ene (**R2**) and Rh-trifluoropyuvate complex (**M1**$_{exo}$) are the key factors that control the stereoselectivity. The analysis of global reactivity indexes of the reactants before and after the catalyst absorption reveals the role of the catalyst by strengthening the nucleophilicity of the reactant **R1** and thus decreasing the energy barrier of the carbonyl-ene reaction. Therefore, this work should be helpful for not only understanding the role of Lewis acid in this kind of reaction but also providing valuable clue for rational design of potent catalysts for synthesizing homoallylic alcohols with high stereoselectivity.

Acknowledgements

We acknowledge financial supports from the National Natural Science Foundation of China (No. 21303167), China Postdoctoral Science Foundation (No. 2013M530340 and 2015T80776), and Excellent Doctoral Dissertation Engagement Fund of Zhengzhou University in 2014.

References

1. K. Mikami and M. Shimizu, *Chem. Rev.*, 1992, **92**, 1021-1050.
2. (a) B. B. Snider, *Acc. Chem. Res.*, 1980, **13**, 426-432; (b) B. B. Snider and E. Ron, *J. Am. Chem. Soc.*, 1985, **107**, 8160-8164; (c) R. J. Loncharich and K. N. Houk, *J. Am. Chem. Soc.* , 1987, **109**, 6947-6952; (d) L. R. Domingo, *Org. Chem. Curr. Res.* , 2013, **2**, 120-126.
3. D. Tymann, A. Kluppel, W. Hiller and M. Hiersemann, *Org. Lett.*, 2014, **16**, 4062-4065.
4. K. Maruoka, Y. Hoshino, T. Shirasaka and H. Yamamoto, *Tetrahedron Lett.*, 1988, **29**, 3967-3970.
5. (a) K. Mikami, M. Terada and T. Nakai, *J. Am. Chem. Soc.*, 1989, **111**, 1940-1941; (b) K. Mikami, M. Terada and T. Nakai, *J. Am. Chem. Soc.*, 1990, **112**, 3949-3954; (c) M. Terada, S. Matsukawa and K. Mikami, *J. Chem. Soc., Chem. Comm.*, 1993, 327-328.
6. D. A. Evans, S. W. Tregay, C. S. Burgey, N. A. Paras and T. Vojkovsky, *J. Am. Chem. Soc.*, 2000, **122**, 7936-7943.
7. K. Zheng, J. Shi, X. Liu and X. Feng, *J. Am. Chem. Soc.*, 2008, **130**, 15770-15771.
8. X. Wang, C. Weigl and M. P. Doyle, *J. Am. Chem. Soc.*, 2011, **133**, 9572-9579.
9. (a) J. Hao, M. Hatano and K. Mikami, *Org. Lett.*, 2000, **2**, 4059-4062; (b) A. Bugarin and B. T. Connell, *Organometallics*, 2008, **27**, 4357-4369; (c) T. Kimura and Y. Uozumi, *Organometallics*, 2008, **27**, 5159-5162; (d) A. Bugarin and B. T. Connell, *J. Chem. Soc. Chem. Comm.*, 2011, **47**, 7218-7220.
10. M. Stol, D. J. M. Snelders, M. D. Godbole, R. W. A. Havenith, D. Haddleton, G. Clarkson, M. Lutz, A. L. Spek, G. P. M. van Klink and G. van Koten, *Organometallics*, 2007, **26**, 3985-3994.
11. J. Ito, K. Fujii and H. Nishiyama, *Chem. Eur. J.*, 2013, **19**, 600-604.
12. J. S. Fossey and C. J. Richards, *Organometallics*, 2004, **23**, 367-373.
13. (a) S. Hosokawa, J. Ito and H. Nishiyama, *Organometallics*, 2012, **31**, 8283-8290; (b) C. P. Owens, A. Varela-Alvarez, V. Boyarskikh, D. G. Musaev, H. M. L. Davies and S. B. Blakey, *Chem. Sci.*, 2013, **4**, 2590-2596.

14. K. Morisaki, M. Sawa, J. Nomaguchi, H. Morimoto, Y. Takeuchi, K. Mashima and T. Ohshima, *Chem. Eur. J.*, 2013, **19**, 8417-8420.
15. T. Wang, X. Q. Hao, J. J. Huang, J. L. Niu, J. F. Gong and M. P. Song, *J. Org. Chem.*, 2013, **78**, 8712-8721.
16. Q. W. Yang, X. L. Tong and W. Q. Zhang, *J. Mol. Struc. THEOCHEM*, 2010, **957**, 84-89.
17. M. Yamanaka and K. Mikami, *Helv Chim. Acta.*, 2002, **85**, 4264-4271.
18. I. Fernandez and F. M. Bickelhaupt, *J. Comput. Chem.*, 2012, **33**, 509-516.
19. D. A. Singleton and C. Hang, *J. Org. Chem.*, 2000, **65**, 895-899.
20. M. Morao, J. P. McNamara and A. H. Hillier, *J. Am. Chem. Soc.*, 2003, **125**, 628-629.
21. (a) L. Zhang and D. C. Fang, *J. Org. Chem.*, 2013, **78**, 2405-2412; (b) W. J. Zhang, D. H. Wei and M. S. Tang, *J. Org. Chem.*, 2013, **78**, 11849-11859; (c) Y. Li and D. C. Fang, *Phys. Chem. Chem. Phys.*, 2014, **16**, 15224-15230; (d) Z. Y. Li, D. H. Wei, Y. Wang, Y. Y. Zhu and M. S. Tang, *J.Org. Chem.*, 2014, **79**, 3069-3078; (e) Y. Wang, D. H. Wei, Z. Y. Li, Y. Y. Zhu and M. S. Tang, *J. Phys. Chem. A*, 2014, **118**, 4288-4300; (f) Y. Wang, D. H. Wei, W. J. Zhang, Y. Y. Wang, Y. Y. Zhu, Y. Jia and M. S. Tang, *Org. Biomol. Chem.*, 2014, **12**, 7503-7514; (g) M. M. Zhang, D. H. Wei, Y. Wang, S. J. Li, J. F. Liu, Y. Y. Zhu and M. S. Tang, *Org. Biomol. Chem.*, 2014, **12**, 6374-6383; (h) Y. Wang, X. K. Guo, M. S. Tang and D. H. Wei, *J. Phys. Chem. A*, 2015, **119**, 8422-8431; (i) Y. Wang, L. J. Zheng, D. H. Wei and M. S. Tang, *Org. Chem. Front.*, 2015, **2**, 874-884; (j) C. H. Geng, S. J. Zhang, C. G. Duan, T. X. Lu, R. X. Zhu and C. B. Liu, *RSC Adv.*, 2015, **5**, 80048-80056; (k) Z. H. Yang and J. X. Xu, *RSC Adv.*, 2015, **5**, 78396-78405; (l) Y. Zhang, Z. H. Qi, G. Y. Ruan, Y. Zhang, W. Liu and Y. Wang, *RSC Adv.*, 2015, **5**, 71586-71592.
22. (a) D. H. Wei, L. Fang, M. S. Tang and C. G. Zhan, *J. Phys. Chem. B*, 2013, **117**, 13418-13434; (b) D. H. Wei, X. Q. Huang, J. J. Liu, M. S. Tang and C. G. Zhan, *Biochemistry-Us*, 2013, **52**, 5145-5154; (c) D. H. Wei, M. S. Tang and C. G. Zhan, *Org. Biomol. Chem.*, 2015, **13**, 6857-6865; (d) Z. Y. Chen, Y. Li, Y. Feng, L. Chen and Q. P. Yuan, *RSC Adv.*, 2015, **5**, 76040-76047; (e) D. M. Li, Y. Wang and K. L. Han, *Coord. Chem. Rev.*, 2012, **256**, 1137-1150; (f) D. M. Li, X. Q. Huang, K. L. Han and C. G. Zhan, *J. Am. Chem. Soc.*, 2011, **133**, 7416-7427; (g) X. K. Guo, L. B. Zhang, D. H. Wei and J. L. Niu, Chem. Sci., 2015, DOI: 10.1039/C5SC01807B.
23. (a) A. Woszczyk and P. Szabelski, *RSC Adv.*, 2015, **5**, 81933-81942; (b) K. Zhang, S. M. Sun and H. Zhang, *RSC Adv.*, 2015, **5**, 81153-81161; (c) S. F. Ma, D. C. Fang, B. M. Ning, M. F. Li, L. He and B. Gong, *Chem. Comm.*, 2014, **50**, 6475-6478; (d) Y. M. Chen, G. A. Chass and D. C. Fang, *Phys. Chem. Chem. Phys.*, 2014, **16**, 1078-1083; (e) M. Gao, G. Q. Gao, Q. Z. Li, X. Yang, W. Z. Li and J. B. Cheng, *RSC Adv.*, 2015, **5**, 76912-76918; (f) M. Hamzehloueian, Y. Sarrafi and Z. Aghaei, *RSC Adv.*, 2015, **5**, 76368-76376.
24. M. J. Frisch, G. W. Trucks, H. B. Schlegel, G. E. Scuseria, M. A. Robb, J. R. Cheeseman, G. Scalmani, V. Barone, B. Mennucci, G. A. Petersson, H. Nakatsuji, M. Caricato, X. Li, H. P. Hratchian, A. F. Izmaylov, J. Bloino, G. Zheng, J. L. Sonnenberg, M. Hada, M. Ehara, K. Toyota, R. Fukuda, J. Hasegawa, M. Ishida, T. Nakajima, Y. Honda, O. Kitao, H. Nakai, T. Vreven, J. A. Montgomery, Jr., J. E. Peralta, F. Ogliaro, M. Bearpark, J. J. Heyd, E. Brothers, K. N. Kudin, V. N. Staroverov, R. Kobayashi, J. Normand, K. Raghavachari, A. Rendell, J. C. Burant, S. S. Iyengar, J. Tomasi, M. Cossi, N. Rega, J. M. Millam, M. Klene, J. E. Knox, J. B. Cross, V. Bakken, C. Adamo, J. Jaramillo, R. Gomperts, R. E. Stratmann, O. Yazyev, A. J. Austin, R. Cammi, C. Pomelli, J. W. Ochterski, R. L. Martin, K. Morokuma, V. G. Zakrzewski, G. A. Voth, P. Salvador, J. J. Dannenberg, S. Dapprich, A. D. Daniels, Ö. Farkas, J. B. Foresman, J. V. Ortiz, J. Cioslowski, and D. J. Fox, *Gaussian, Inc.*,

Wallingford CT, 2009.

25. (a) C. Lee, W. Yang and R. G. Parr, *Phys. Rev. B*, 1988, **37**, 785-789; (b) A. D. Becke, *J. Chem. Phys.*, 1993, **98**, 5648-5652.

26. (a) P. Fuentealba, H. Preuss, H. Stoll and L. v. Szentpály, *Chem. Phys. Lett.*, 1982, **89**, 418-422; (b) P. Fuentealba, H. Stoll, L. v. Szentpály, P. Schwerdtfeger and H. Preuss, *J. Phys. B*, 1983, **16**, L323-L328.

27. A. V. Marenich, C. J. Cramer and D. G. Truhlar, *J. Phys. Chem. B*, 2009, **113**, 6378-6396.

28. (a) C. Gonzalez and H. B. Schlegel, *J. Chem. Phys.*, 1989, **90**, 2154-2161; (b) C. Gonzalez and H. B. Schlegel, *J. Phys. Chem.*, 1990, **94**, 5523-5527.

29. (a) E. D. Glendening, A. E. Reed, J. E. Carpenter, and F. J. Weinhold, *NBO Version 3.1*; (b) J. P. Foster and F. J. Weinhold, *J. Am. Chem. Soc.*, 1980, **102**, 7211-7218; (c) A. E. Reed and F. J. Weinhold, *J. Chem. Phys.*, 1983, **78**, 4066-4073.

30. C. Y. Legault, *CYLview, 1.0b; Université de Sherbrooke, 2009 (http://www.cylview.org)*.

31. (a) A. Schaefer, H. Horn and R. Ahlrichs, *J. Chem. Phys.*, 1992, **97**, 2571-2577; (b) A. Schaefer, C. Huber and R. Ahlrichs, *J. Chem. Phys.*, 1994, **100**, 5829-5835.

32. S. Grimme, S. Ehrlich and L. Goerigk, *J. Comput. Chem.*, 2011, **32**, 1456-1465.

33. Y. Zhao and D. G. Truhlar, *J. Chem. Phys.*, 2006, **125**, 194101-194118.

34. (a) C. J. Christopher and D. G. Truhlar, *Phys. Chem. Chem. Phys.*, 2009, **11**, 10757-10816; (b) X. F. Xu, P. Liu, A. Lesser, L. E. Sirois, P. A. Wender and K. N. Houk, *J. Am. Chem. Soc.*, 2012, **134**, 11012-11025; (c) T. Sperger, I. A. Sanhueza, I. Kalvet and F. Schoenebeck, *Chem. Rev.*, 2015, **115**, 9532-9586.

35. (a) Y. Qiao and K. L. Han, *Org. Biomol. Chem.*, 2014, **12**, 1220-1231; (b) Y. Qiao and K. L. Han, *Org. Biomol. Chem.*, 2012, **10**, 7689-7706.

36. C. Y. Legault, Y. Garcia, C. A. Merlic and K. N. Houk, *J. Am. Chem. Soc.*, 2007, **129**, 12664-12665.

37. R. G. Parr and R. G. Pearson, *J. Am. Chem. Soc.*, 1983, **105**, 7512-7516.

38. (a) L. R. Domingo, J. A. Saez, R. J. Zaragoza and M. Arno, *J. Org. Chem.*, 2008, **73**, 8791-8799; (b) L. R. Domingo, M. T. Picher and J. A. Saez, *J. Org. Chem.*, 2009, **74**, 2726-2735; (c) L. R. Domingo, M. J. Aurell, P. Perez and R. Contreras, *Tetrahedron*, 2002, **58**, 4417-4423.

39. (a) W. Kohn and L. J. Sham, *Phys. Rev.*, 1965, **137**, 1697-1705; (b) L. J. Sham and W. Kohn, *Phys. Rev.*, 1966, **145**, 561-567.

40. (a) L. R. Domingo, E. Chamorro and P. Perez, *J. Org. Chem.*, 2009, 3036-3044; (b) L. R. Domingo, E. Chamorro and P. Perez, *J. Phys. Chem. A*, 2008, **112**, 4046-4053; (c) L. R. Domingo, P. Perez and J. A. Saez, *RSC Adv.*, 2013, **3**, 1486-1494; (d) E. Chamorro, P. Perez and L. R. Domingo, *Chem. Phys. Lett.*, 2013, **582**, 141-143.

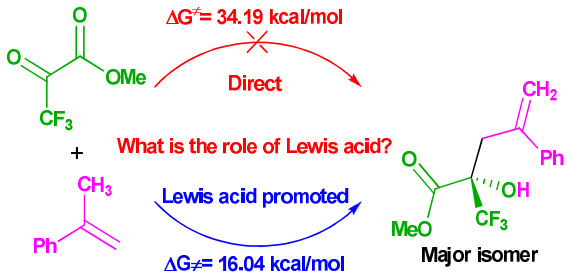

The mechanism and stereoselectivity of the Lewis acid catalyzed carbonyl-ene of trifluoropyuvates with arylpropenes have been investigated using DFT method.